Applied Physics B (2025) 131:146
https://doi.org/10.1007/s00340-025-08490-3

Applied Physics B
Lasers and Optics

RESEARCH

A practical guide to feedback control for Pound–Drever–Hall laser linewidth narrowing

Wance Wang[1] · **Sarthak Subhankar**[1,2] · **Joseph W. Britton**[1,3]

Received: 20 March 2025 / Accepted: 13 May 2025

Abstract
The Pound–Drever–Hall (PDH) technique for laser linewidth narrowing is widely used by AMO experimentalists. However, achieving a high-performance PDH locking requires substantial engineering experience, which is scattered across literature and often lacks a cohesive control-theory perspective. Excellent pedagogical papers exist on the theory of the PDH error signal (Black in Am J Phys 69:79, 2000; Day et al. in IEEE J Quantum Electron 28:1106, 1992; Thorpe et al. in Opt Express 16:15980, 2008; Reinhardt et al. in Opt Express 25:1582, 2017), but they rarely cover feedback control. General-purpose control theory literature (Bechhoefer in Rev Mod Phys 77:783, 2005; Ogata in Modern control engineering. Pearson Education, London, 2010) seldom discusses PDH laser locking specifically. Although excellent PDH review articles (Hall et al. in Handbook of optics. McGraw-Hill Professional, New York, 1999; Fox et al. in Stabilizing diode lasers to high-finesse cavities. National Institute of Standards and Technology, Boulder 2003; Nagourney in Quantum electronics for atomic physics and telecommunication. Oxford University Press, Oxford 2014) provide thorough knowledge and practice on both aspects, they are not novice-friendly. We extend prior works (Hall et al. 1999; Fox et al. 2003; Nagourney 2014) by addressing component choice and loop tuning using modern tools like a vector network analyzer. We organize multifaceted engineering considerations systematically, grounded in feedback control principles. Our target reader is researchers setting up a PDH laser lock for the first time; we eschew advanced topics like minimizing residual amplitude modulation (RAM). Our guidance is illustrated by step-by-step optimization of the lock for a 1650 nm ECDL.

1 Introduction

The PDH optical frequency analyzer plays a central role in closed-loop laser frequency stabilization and laser linewidth narrowing [10]. The technique enables ultra-narrow line width lasers [11–16], record-setting optical atomic clocks [17–23] and high-resolution spectroscopy [24–26]. Researchers at the forefront of laser stabilization can now build ultra-narrow, high-stability cavities [12, 27–32] and reduce effects like residual amplitude modulation (RAM) [33–36] to obtain stabilization at the mHz level [16, 37]. It is our observation that many of the techniques used by expert practitioners to obtain these impressive results are not well documented. We hope this tutorial partially bridges this gap and broadens the accessibility of laser frequency stabilization techniques.

2 Just enough control theory

We start with a brief introduction to feedback control theory and omit details extraneous to the aim of first-order PDH optimization. Excellent general-purpose control tutorials include those by Bechhoefer [5], Ogata [6], and Doyle [38]. While preparing this manuscript, we noted another excellent summary of both control theory and the PDH technique by Oswald [39].

2.1 The feedback loop

Our system consists of a collection of components and signals. All components are linear and time-invariant (LTI).

✉ Wance Wang
wwcphy@umd.edu

[1] Department of Physics, University of Maryland, College Park, MD 20742, USA

[2] Joint Quantum Institute, National Institute of Standards and Technology, College Park, MD, USA

[3] U.S. Army Combat Capabilities Development Command, Army Research Laboratory, Adelphi, MD 20783, USA

Published online: 24 June 2025

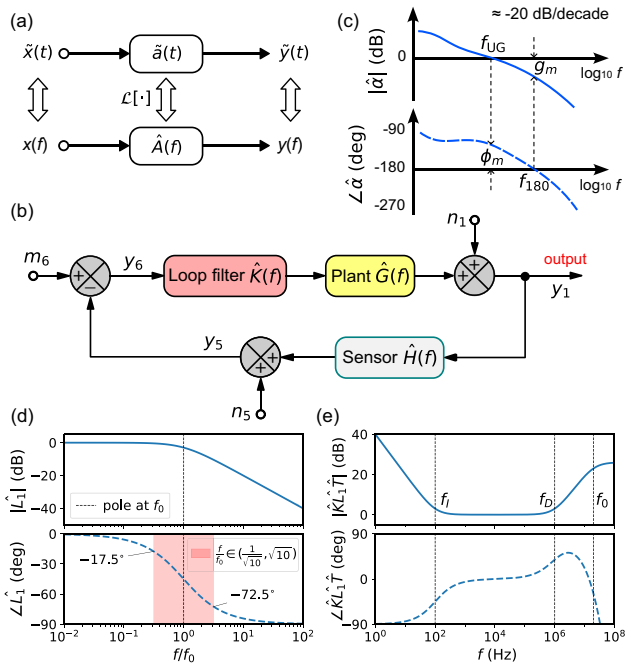

Fig. 1 **a** $\tilde{a}$ is a time-invariant (LTI) system component that transforms signal $\tilde{x}$ to $\tilde{y}$. The transfer function $\hat{A}$ encodes the frequency-domain behavior of $\tilde{a}$. **b** The block diagram illustrates a feedback loop. Components of the loop include a plant $\hat{G}$, sensor $\hat{H}$ and loop filter $\hat{K}$. Signals decorated by integers include observable y_k, noise n_k and modulation m_k signals. **c** A Bode plot for a sample open-loop transfer function $\hat{\alpha}$. By convention the gain is plotted in dB ($20\log_{10}|\hat{\alpha}|$) and the frequency is $\log_{10} f$. Dashed lines call out the *unity-gain* (UG) point f_{UG}, *phase margin* ϕ_m, *phase crossover* point f_{180} and *gain margin* g_m. **d** The first-order low-pass filter $\hat{L}_1$ with corner frequency f_0. It's properties include 3 dB attenuation and a −45° phase lag at f_0. 60% of the phase change occurs in the one decade around f_0 (red). **e** A sample plot of a PID loop filter $\hat{K}\hat{L}_1\hat{T}$ transfer function where $\hat{K}$ is given by Eq. (6), $K_P = 1$, $f_I = 100$ Hz, and $f_D = 1$ MHz. In the high-frequency limit all devices are ultimately bandwidth-limited and exhibit low-pass behavior, corner frequency $f_0 = 20$ MHz for $\hat{L}_1$ and delay $\tau_l = 10$ ns for $\hat{T}$

Component $\tilde{a}(t)$ transforms an input signal $\tilde{x}(t)$ to an output signal $\tilde{y}(t)$. Their relation is simple in Laplace domain

$$\hat{A} = y/x. \tag{1}$$

$\hat{A}(f) = \mathscr{L}[\tilde{a}(t)]$ is called the transfer function of the component (Fig. 1a) and we set the complex variable $s = j2\pi f$. We use the $\sim$ symbol for time-domain signals and $\hat{}$ symbol for transfer functions. To reduce clutter we often omit the $\hat{}$ for Laplace-domain signals $x(f) = \mathscr{L}[\tilde{x}(t)]$ and the explicit time or frequency dependence. The magnitude and phase of $\hat{A}$ are denoted by $|\hat{A}|$ and $\angle\hat{A}$, respectively. As f increases, the change in $\angle\hat{A}$ is called the *phase shift*. When $\angle\hat{A} > 0$ it is *phase lead* and when $\angle\hat{A} < 0$ it is *phase lag*. A vector network analyzer (VNA) is a tool used in system discovery: by driving x and observing y we learn about $\hat{A}$. It is common to visualize transfer functions with a Bode plot (Fig. 1c).

To implement a feedback control system, components are connected as a loop. The loop signals $\tilde{y}_k(t)$ can represent a range of physical quantities including electrical (in volts) and optical frequency (in Hz). In frequency domain, $y_k = \mathscr{L}[\tilde{y}_k(t)]$. A block diagram (Fig. 1b) is a pictorial representation of transfer functions and signals y_k, where k labels the signal position in the block diagram. Common loop components are the plant $\hat{G}$, sensor $\hat{H}$ and loop filter $\hat{K}$. We call signal y_1 the *output signal* and y_5 the *error signal*. The signal m_6 is an external input. We represent noise in the plant and sensor as signals n_1 and n_5 (Fig. 1d).

The open-loop transfer function is the product of all loop components [9]

$$\hat{\alpha} = \hat{K}\hat{G}\hat{H} \tag{2}$$

The closed-loop transfer function is the ratio of error signal y_5 to m_6

$$\frac{y_5}{m_6} = \frac{\hat{K}\hat{G}\hat{H}}{1+\hat{K}\hat{G}\hat{H}} = \frac{\hat{\alpha}}{1+\hat{\alpha}} \tag{3}$$

If we add noises n_1 and n_5, the output becomes

$$y_1 = \frac{\hat{\alpha}}{1+\hat{\alpha}}\left(\frac{m_6}{\hat{H}} + \frac{n_1}{\hat{\alpha}} - \frac{n_5}{\hat{H}}\right) \tag{4}$$

The power spectral density (PSD) is

$$S_{y1} = \frac{1}{|1+\hat{\alpha}|^2}S_{n1} + \frac{|\hat{\alpha}|^2}{|1+\hat{\alpha}|^2}\frac{1}{\left|\hat{H}\right|^2}S_{n5} \tag{5}$$

where S_{n1} and S_{n5} are the noise PSD.

Ideal *negative feedback* is characterized by a loop where $|\hat{\alpha}| \to \infty$ while $\angle\hat{\alpha} = 0°$ at all frequencies of interest. In this case we have strong suppression of n_1: $y_1 = (m_6 - n_5)/\hat{H}$. However, there is no suppression of n_5. This tension between high gain reducing laser noise but increasing susceptibility to measurement noise will be a recurring theme.

If at any frequency $|\hat{\alpha}(f)| > 1$ and $\angle\hat{\alpha}(f) < -150°$, the loop amplifies noise and may be unstable. Given the central role of $\hat{\alpha}$ in loop performance, the control community has developed terminologies to describe loop stability [6] (see Fig. 1c). The *unity-gain* (UG) point f_{UG} is the frequency where $|\hat{\alpha}(f_{\mathrm{UG}})| = 0\,\mathrm{dB}$[1] and the *phase margin* is $\phi_m = 180° + \angle\hat{\alpha}(f_{\mathrm{UG}})$. At f_{UG} with an empirical $\phi_m = 60°$, the factor $1/|1+\hat{\alpha}|^2 = 1$ in Eq. (5), so the loop has no suppression on the noise spectrum S_{n1} when $f > f_{\mathrm{UG}}$. The *phase crossover* point f_{180} is the frequency where $\angle\hat{\alpha}(f_{180}) = -180°$ and *gain margin* is $g_m = 1/|\hat{\alpha}(f_{180})|$. A consequence of

[1] f_{UG} is also called "loop bandwidth" [40].

negative feedback is increased sensitivity to noise called the *servo bump* [41], which commonly occurs over the range $f_{\mathrm{UG}} < f < f_{180}$. We define f_{bump} to be the frequency where servo bump noise spectral density is a maximum.[2]

2.2 Loop components

Now we introduce some components found in PDH laser locks (Fig. 1b).

Plant The plant is a laser. We define the laser optical frequency (in Hz) to be $\tilde{y}_1 + \nu_c$, where ν_c is an optical cavity resonance (at an optical frequency) and $\tilde{y}_1$ is the laser-cavity detuning (at a RF frequency). The signal $y_1 = \mathscr{L}[\tilde{y}_1]$ is the Laplace transform of the laser detuning and n_1 is its frequency noise.

Sensor We need a sensor that transforms frequency signal $\tilde{y}_1$ into voltage signal $\tilde{y}_5$. Here we focus on the cavity-based PDH optical frequency discriminator (the "PDH discriminator") [1, 7]. This sensor measures an optical frequency relative to an internal, non-adjustable frequency ν_c (the nearest cavity transmission feature). Its output is a voltage $\tilde{y}_5 \propto \tilde{y}_1$ and its transfer function is $\hat{H}_{\nu_c}$. Another property of $\hat{H}_{\nu_c}$ is that it's output is linear only for $\tilde{y}_1 \in (-\delta\nu_c/2, \delta\nu_c/2)$, where $\delta\nu_c$ is the cavity optical linewidth (Fig. 2b). Note that outside this bandwidth the LTI assumption fails. Measuring $\hat{H}_{\nu_c}$ directly is non-trivial as many lasers require active feedback to remain within $\nu_c \pm \delta\nu_c/2$ – we will return to this topic later.

Loop filter The transfer function of a loop filter $\hat{K}$ is tailored to advance feedback design goals. The proportional–integral–derivative (PID) loop filter is widely-used

$$\hat{K} = K_P\left(1 - j\frac{f_I}{f} + j\frac{f}{f_D}\right) \tag{6}$$

where K_P is proportional gain, f_I, f_D are the P–I and P–D corner frequencies, respectively (Fig. 1d). The second term is an integrator (I) with gain slope −20 dB per decade that adds −90° phase lag when $f \ll f_I$. The third term is a differentiator (D) with gain slope +20 dB per decade that adds +90° phase lead when $f \gg f_D$. We adjust the phase lag of $\hat{K}$ by tuning f_I and f_D. The UG point can be extended by using the up to +90° phase lead available from the D term.[3] The control available from PID is usually enough but some lasers may benefit from more sophisticated feedback [42].

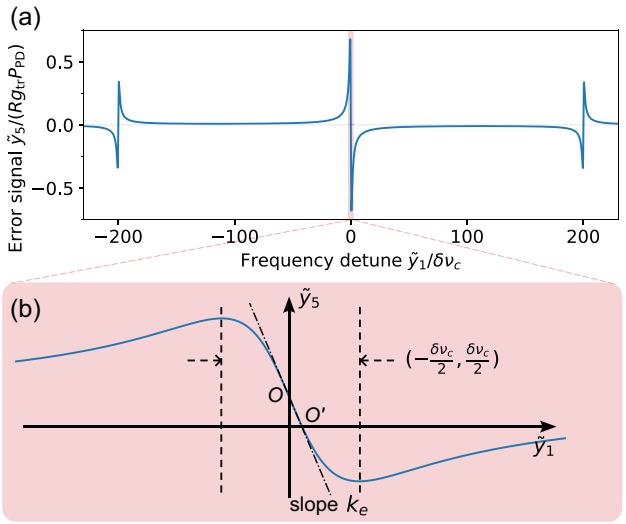

Fig. 2 **a** A sample PDH error signal for $\delta\nu_c = 100$ kHz, $\Omega/2\pi = 20$ MHz and $\beta = 1.082$. $\tilde{y}_1$ and $\tilde{y}_5$ are instantaneous laser frequency detuning and error signal in time domain. **b** Zoom-in of the red-shaded area in **a**. Signal $\tilde{y}_5$ is linear only over a narrow region $\tilde{y}_1 \in (-\delta\nu_c/2, \delta\nu_c/2)$. Ideally the signal is symmetric about the zero crossing point O. Here we show an offset error: $\tilde{y}_5 = 0$ is at O'

Delay An implicit element of any feedback loop is propagation delay τ_l. The transfer function is $\hat{T} = \exp(-j2\pi f\tau_l)$ which has magnitude 1 and a phase that increases linearly in f without bound. The phase delay $2\pi f\tau_l$ is fundamental and can't be corrected by other loop components. At high frequency, the phase lag due to $\hat{T}$ can limit f_{UG} and feedback performance. For example, the phase lag is 18° at $f = 1$ MHz if the loop length is 10 m in coaxial cables. The transfer function $\hat{T}$ does not explicitly appear in block diagrams as it is distributed across all components.

Simple models for these components include the following.

First-order low-pass The low-pass filter is a common loop element that results in a phase shift. The transfer function for a first-order low-pass is (Fig. 1d),

$$\hat{L}_1 = \frac{1}{1 + jf/f_0} \tag{7}$$

where f_0 is the corner frequency. The attenuation of $\hat{L}_1$ at f_0 is $-3dB$ and for $f > f_0$ the slope is $-20dB$/decade. The phase shift is $\angle\hat{L}_1 = -\arctan(f/f_0)$. Notice that $\angle L_1(f_0)$ is −45° and it has the steepest change in the decade $(1/\sqrt{10}, \sqrt{10})f_0$. The electronic RC circuit is an example of a first-order low-pass where $f_0 = 1/(2\pi RC)$.

high-order low-pass Later we will encounter a need for higher-order low-pass filters $\hat{L}_n$ with corner f_0, and where $\lim_{f\to\infty} \angle\hat{L}_n = -90° \times n$ [9]. The common n-th

[2] If the S_{n5} term in Eq. (5) is ignored, the position of f_{bump} is where $|1 + \hat{\alpha}|^2$ is minimum so S_{y1} is maximized.

[3] Real-world PID devices often fall short of the full +90° phase lead available from an ideal D term. See the plot Fig. 1e.

order Butterworth low-pass $\widehat{LB}_n$ has slope $-20\,\text{dB} \times n$ per decade for $f > f_0$. At intermediate frequencies $\angle\widehat{LB}_n$ can be computed numerically [43] or approximated by $\angle\widehat{LB}_n \approx -n \arctan(f/f_0)$. Strong attenuation comes at the cost of large phase lag – the right filter is context dependent. All real-world plants $\hat{G}$ exhibit low-pass behavior at high frequency and can be approximated by some low-pass $\hat{L}_n$.

2.3 Feedback design goals

Here we provide advice for choosing feedback parameters in simple closed-loop systems. Our high-level design goals are the following:

1. maximize f_{UG}
2. maintain $30° < \phi_m < 60°$
3. for $f < f_{\text{UG}}$, maintain $\angle\hat{\alpha} > -120°$

Naturally, for $f < f_{\text{UG}}$ we also want to maximize $|\hat{\alpha}|$. However, this aim is constrained by a gain-phase relationship first considered by Bode [5, 44], a special case of the Kramers–Kronig relation [45].

For a transfer function $\hat{A}$[4], phase $\angle\hat{A}$ is uniquely related to gain $|\hat{A}|$. When the slope of $20\log_{10}|\hat{A}(f)|$ is $-n$, the phase $\angle\hat{A}(f) \approx -n \times 90°$.

This relation dictates that the open-loop gain $|\hat{\alpha}|$ should decrease by at most −20 dB/decade to avoid $\angle\hat{\alpha} < -150°$; note that our design goals 2 and 3 are even more strict constraints in the interest of maintaining loop stability. This rationalizes our first design goal: because the slope of $|\hat{\alpha}|$ is constrained, the only way to obtain large $|\hat{\alpha}|$ is to maximize f_{UG}. A corollary is that the primary way to add phase lead near f_{UG} is to increase $|\hat{\alpha}|$. Because of the phase lag in Fig. 1d, in many cases the highest achievable f_{UG} is one decade lower than f_0 for the dominant low-pass in the loop. Note that the feedback can be made more robust to long-term drift in $|\hat{\alpha}|$ by minimizing the slope $d\angle\hat{\alpha}/df$ near f_{UG}.

Two key trade-offs should be considered when tuning the loop phase margin. First, an increase in $|\hat{\alpha}|$ is accompanied by a reduction in ϕ_m. That is, better suppression of noise n_1 in one frequency band comes at the cost of loop instability and stronger servo bump in another. Second, small ϕ_m provides fast transient response but suffers from increased ringing and overshoot. In practice, empirical range $30° < \phi_m < 60°$ is recommended for satisfactory performance [6].

The last design goal ensures stability for all $f < f_{\text{UG}}$. The Ziegler-Nichols method [6] is an algorithm for tuning PID parameters that respects these design goals but is typically not optimal – we return to this topic in Sect. 4.1.

3 PDH lock component choices

In this section we discuss a laser frequency stabilization system containing a PDH optical frequency discriminator (OFD) $\hat{H}_{v_c}$ and provide advice on component choices. The system consists of loop signals y_k and the following components (Fig. 5a): a laser to be stabilized, an electro-optic modulator (EOM), an optical reference cavity, a photodetector (PD), RF demodulation electronics and a loop filter. For details on the PDH frequency discriminator itself, the reader is referred to Ref. [1] and Sect. 3.2.4.

3.1 Laser

To be concrete we consider a generic external-cavity diode laser (ECDL). Output signal y_1 is the laser frequency which is modulated by two actuators: laser diode current (the *fast branch*) and grating diffraction angle modulated by PZT (the *slow branch*). Each feedback path can be modeled by its own open-loop transfer function ($\hat{G}_{\text{fast}}$ and $\hat{G}_{\text{slow}}$) with laser-limited low-pass corner frequencies ($f_{0,\text{fast}}$ and $f_{0,\text{slow}}$). The high-pass corner frequency of the *fast branch* is $f_{\text{HP,fast}}$, typically set by the laser diode head board [46].

We assume a simple model for free-running laser frequency noise [9, 47, 48]. Let $S_{n1}(f)$ be the frequency noise PSD (Hz^2/Hz) [9]. This quantity can be calculated from the auto-correlation $R_\phi(t)$ of the laser phase over time $\phi(t)$.

$$R_\phi(\tau) = \lim_{T\to\infty} \frac{1}{T} \int_{T/2}^{T/2} \phi(t+\tau)\phi(t)dt \tag{8}$$

$$S_{n1}(f) = \frac{1}{2\pi} f^2 \int_{\infty}^{\infty} R_\phi(\tau) e^{i2\pi f\tau} d\tau \tag{9}$$

Free-running laser noise can be parameterized as

$$S_{n1}(f) = h_{-1} f^{-1} + h_0 f^0 \tag{10}$$

where h_{-1} is the 1-Hz-frequency intercept for 1/*f*-noise and h_0 is the the 1-Hz-frequency intercept for white frequency noise. The instantaneous laser linewidth is dominated by the white noise and has a Lorentzian line shape with πh_0 full-width at half-max. The β-separation method [47] is a technique for estimating the linewidth for noise spectra that do not necessarily follow Eq. (10). We note that a single linewidth number can be quite misleading [8, 48–50]; we recommend obtaining the spectrum $S_{n1}(f)$ from laser manufacturers prior to purchasing a laser and PDH stabilization components (especially the reference cavity).

[4] $\hat{A}$ has to be minimum-phase [45]

Although we focus on ECDL in this work, the description here captures features that can be similar in other types of lasers. For background on other laser types, readers may refer to Ref. [9, 28].

We recommend the following properties for an ECDL to be easily PDH-stabilized:

- $f_{0,\text{fast}}$ is at least one decade higher than the noise that one wants to suppress
- $f_{\text{HP,fast}}$ should be lower than $f_{0,\text{slow}}/10$

The first is motivated by the observation that $f_{\text{UG}} \sim f_{0,\text{fast}}/10$. Further, since f_{UG} is often limited to ~ 2 MHz by loop propagation delay, we recommend $f_{0,\text{fast}} > 10$ MHz. However, too strong $S_{n1}(f)$ may still preclude stable laser locking even though f_{UG} is faster than the noise, see our analysis in Ref. [51].

Distinct fast- and slow-modulation inputs are present in most laser systems. For many laser types the slow feedback path $\hat{G}_{\text{slow}}$ has many resonances as it is effected by PZT actuation of mechanical components like mirrors or gratings [52, 53]. The second is motivated by the observation that feedback via $\hat{G}_{\text{fast}}$ needs to suppress the slow branch servo bump so we require $f_{\text{HP,fast}} < f_{0,\text{slow}}/10$. Note that advanced techniques that can eliminate the servo bump altogether [41].

3.2 PDH frequency discriminator

Generation of the PDH error signal $\tilde{y}_5$ relies on several components which can be independently optimized.

3.2.1 Modulation and demodulation

An EOM driven at RF frequency Ω is used to add side bands to the laser. An RF mixer demodulates the PD output using Ω applied to the LO port of a mixer. There is a low-pass filter downstream of the mixer with corner frequency f_M that outputs signal $\tilde{y}_5$. The demodulation transfer function (mixer+low-pass) is $\hat{D}$.

Common choices for $\Omega/2\pi$ are 10 to 20 MHz [13, 33, 54, 55]. Resonant EOMs operate at a single manufacturer-defined frequency, while fiber-EOMs have roughly uniform response from 1 MHz to beyond 10 GHz, they have lower power handling. For for laser light at frequency $\tilde{y}_1$ the EOM output is $\exp(j2\pi\tilde{y}_1 t + j\beta\sin(\Omega t))$ which can be expanded as

$$e^{j2\pi\tilde{y}_1 t}\left(J_0(\beta) + \sum_{k=1}^{\infty} J_k(\beta)e^{jk\Omega t} + \sum_{k=1}^{\infty}(-1)^k J_k(\beta)e^{-jk\Omega t}\right) \quad (11)$$

where β is the modulation depth and J_k is k-th order Bessel function. Mixing of the side bands J_0 and $J_{\pm 1}$ reflected by the optical cavity gives rise to signal $\tilde{y}_5$. If $\beta = 1.082$ the linear region slope k_e (discussed later in Eq. (15)) is maximum. A DC term in $\tilde{y}_4$ is blocked by the RF port of the mixer but 2Ω terms are demodulated to frequency Ω in $\tilde{y}_5$. The desired signal $\tilde{y}_5$ is proportional to $q = 4J_0(\beta)J_1(\beta)$ while unwanted modulation at Ω is proportional to $p = 2J_1(\beta)^2 + 4J_0(\beta)J_2(\beta)$ [1]. A low-pass filter after the mixer blocks the unwanted modulation at the cost of a phase shift that limits f_{UG}.[5] To reach a signal-to-noise ratio (SNR) of 10^3, attenuation $-20\log_{10}(10^3/\frac{q}{p}) \approx -55$ dB is needed at Ω.

Suppose that $\Omega/2\pi = 20$ MHz and $f_{\text{UG}} = 1$ MHz. An n-th order Butterworth filter provides -55 dB attenuation when $f_M = (\Omega/2\pi)10^{-\frac{55}{20n}}$. Numerical results show that the attenuation target is met when $n = 8$ and $f_M = 9$ MHz; the phase lag is $\angle\widehat{LB}_n(f_{\text{UG}}) = -33°$. To reduce the phase lag one has to either increase modulation Ω or sacrifice SNR. Alternative solutions include using a high-Q notch filter at Ω [8] or relying on the loop filter's inherent low-pass characteristics while removing additional filters.

3.2.2 Photodetector

The light detector consists of a photodetector and a transimpedance amplifier. We call this composite device a PD and call its transfer function $\hat{P}$. The relevant properties are its responsivity R (in units of A/W), transimpedance gain g_{tr} (in units of V/A), noise equivalent power (NEP, in units of $\text{W}/\sqrt{\text{Hz}}$) and it's frequency response, modeled as an n-th order low-pass $\hat{L}_{\text{PD}}$ with corner frequency f_{PD}. For incident optical power P_{PD}, the output voltage amplitude at DC is $P_{\text{PD}}Rg_{\text{tr}}$.

Noise in the PD can be consequential to overall PDH performance. Contributions include detector electronic noise (including electronic shot noise) characterized by NEP [56] and photon shot noise [1, 2]. The NEP is defined as the incident power that gives an SNR of one in a 1 Hz bandwidth. For photocurrent, the RMS electronic noise in bandwidth δ is $I_{en} = \text{NEP} \times R\sqrt{\delta}$ and the noise by photon shot noise at power P_{PD} is $I_{sn} = \sqrt{4eRJ_1(\beta)^2 P_{\text{PD}}}\sqrt{\delta}$. The optical power when $I_{en} = I_{sn}$ is $P_{\text{PD}}^{(eq)} = \text{NEP}^2 R/(4eJ_1(\beta)^2)$. The SNR at $P_{\text{PD}}^{(eq)}$ is then

$$\frac{P_{\text{PD}}^{(eq)}R}{I_{en} + I_{sn}} = \frac{\text{NEP}}{8eJ_1(\beta)^2\sqrt{\delta}}R \quad (12)$$

The threshold $P_{\text{PD}} > P_{\text{PD}}^{(eq)}$ is notable since above it electronic noise no longer dominates. In the context of PDH, the bandwidth that contributes to noise in y_5 is $(\Omega/2\pi - f_M, \Omega/2\pi + f_M)$, where f_M is the corner frequency of the low-pass following the mixer. Now we can put some numbers to it: suppose NEP = 10 $\text{pW}/\sqrt{\text{Hz}}$, $R = 1$ A/W

[5] Some loop filters provide sufficient attenuation at Ω and don't require an external low-pass.

and $f_M = 9$ MHz. Then, $P_{\mathrm{PD}}^{(eq)} = 720\mu$W and the SNR is 8480.

In Appendix 6.1, we show that $\hat{P}$ depends on the value of Ω due to the mixer:

$$\hat{P} = e^{\frac{j}{2}[\angle\hat{L}_{\mathrm{PD}}(\Omega+f)-\angle\hat{L}_{\mathrm{PD}}(\Omega-f)]} \tag{13}$$

We see wide variation in the phase response of commercial PD packages that can be approximated by $\angle\hat{L}_{\mathrm{PD}}(f) \approx -n\arctan(f/f_{\mathrm{PD}})$, where n is the number of poles. We find $n = 3$ for several PDs in our lab. Given $\Omega/2\pi = 20$ MHz, $f_{\mathrm{PD}} = 10\Omega/2\pi$ and $f_{\mathrm{UG}} = 1$ MHz, we get $\angle\hat{P}(f_{\mathrm{UG}}) = -0.9°$. An especially sub-optimal choice is $\Omega/2\pi = 5$ MHz and $f_{\mathrm{PD}} = 5$ MHz where $\angle\hat{P}(f_{\mathrm{UG}}) = -17°$.

Given what we've seen so far you might think $\Omega/2\pi > 20$ MHz is an improvement, however it's not so simple. Nonidealities that emerge for such frequencies include the following. (1) The phase lag $\angle\hat{P}$ becomes larger. (2) The electronics for offset-locking becomes marginally harder [3, 57–60]. (3) It is increasingly hard to avoid overlap of EOM sidebands with higher-order transverse cavity modes [61].

3.2.3 Reference cavity

An ultrastable Fabry-Perot optical cavity is commonly used in PDH-based frequency discriminators [9, 28]. Salient cavity properties are it's transmission frequency ν_c, the resonance full width at half max linewidth $\delta\nu_c$ and free spectral range (FSR) ν_{FSR}. The cavity finesse is $\mathscr{F} = \nu_{\mathrm{FSR}}/\delta\nu_c$ and the resonator quality factor is $Q = \frac{c/\lambda}{\delta\nu_c}$. The transfer function for the light reflected by the cavity has a low-pass response

$$\hat{C} = 1/(1 + j2f/\delta\nu_c) \tag{14}$$

[2, 4, 9], where $\delta\nu_c/2$ is the corner frequency. Appendix 6.2 shows how to measure $\delta\nu_c$ by cavity ring-down. Guidance on laser beam alignment to the cavity is in [61, 62].

3.2.4 Discriminator

Now we combine our knowledge of individual components to better understand properties of the PDH frequency discriminator transfer function $\hat{H}_{\nu_c}$. The subscript ν_c reminds us that the reference frequency is defined by the cavity.

A sample PDH error signal is plotted in Fig. 2a. The slope k_e of the discriminator response is [1]

$$k_e := \left.\frac{d\tilde{y}_5}{d\tilde{y}_1}\right|_{\tilde{y}_1=0} = 8J_0(\beta)J_1(\beta)P_{\mathrm{PD}}Rg_{\mathrm{tr}}/\delta\nu_c \tag{15}$$

with units of V/Hz. Note that $\tilde{y}_1$ and $\tilde{y}_5$ are time-domain signals. The overall PDH discriminator transfer function is given by (see Fig. 5b)

$$\hat{H}_{\nu_c} := \frac{y_5}{y_1} \approx \hat{D}\hat{P}k_e\hat{C} \tag{16}$$

and includes terms for demodulation $\hat{D}$, photodetector $\hat{P}$ and cavity $\hat{C}$.

Following are several design goals to optimize $\hat{H}_{\nu_c}$.

- maximize k_e
- choose $\delta\nu_c/2 < 300$ kHz (see Sec. 3.4)
- make $\tilde{y}_5$ symmetric about $\tilde{y}_5 = 0$

We can now write a more detailed expression for the laser frequency detuning

$$y_1 = \frac{\hat{\alpha}}{1+\hat{\alpha}}\left(\frac{n_1}{\hat{\alpha}} - \frac{n_4}{k_e\hat{C}}\right) \tag{17}$$

where $\hat{\alpha} = \hat{\alpha}_{\mathrm{slow}} + \hat{\alpha}_{\mathrm{fast}} = \hat{H}_{\nu_c}\hat{K}_{\mathrm{slow}}\hat{G}_{\mathrm{slow}}\hat{T} + \hat{H}_{\nu_c}\hat{K}_{\mathrm{fast}}\hat{G}_{\mathrm{fast}}\hat{T}$ (see the loop in Fig. 5). As expected laser noise n_1 is suppressed by the loop gain $1 + \hat{\alpha}$ while noise n_4 is only suppressed by $k_e\hat{C}$.

Increasing P_{PD} improves k_e and SNR, but use caution as it can have adverse consequences including heating of mirror coatings, cavity drift [63], error signal asymmetry [8], and cross-talk in a multi-color PDH setup. Finally, maximize k_e by adjusting the phase-delay between the LO and mixer (Fig. 4a). We discuss choice of $\delta\nu_c$ in Sec. 3.4.

Since $\hat{H}_{\nu_c}$ is linear only for $\tilde{y}_1 \in (-\delta\nu_c/2, \delta\nu_c/2)$, care must be exercised during operation to ensure this limit is not violated. A proper error signal is symmetric about $\tilde{y}_5 = 0$. The simplest asymmetry is an offset to the entire error signal. If the offset is slowly varying, the result is a shift in the lock point and reduced discriminator dynamic range. We note that the offset can vary due to RAM [33, 36].[6]

The transfer function $\hat{H}_{\nu_c} = \hat{D}\hat{P}k_e\hat{C}$ is straightforward to determine. $\hat{C}$ is determined by cavity ring-down. The slope k_e is best determined empirically. Increase $|\hat{\alpha}|$ by raising loop filter gain K_P so the error signal $\tilde{y}_5$ oscillates well into saturation. Note the peak to peak amplitude $\tilde{y}_5^{\mathrm{PP}}$ on an oscilloscope and calculate $k_e = 2\tilde{y}_5^{\mathrm{PP}}/\delta\nu_c$. As a first-order approximation, $\hat{D}$ is in many situations dominated by the low-pass filter and $\hat{P} = 1$ in the limit of high PD bandwidth. Precisely, $\hat{D}\hat{P}$ can be measured with a VNA as mentioned in Appendix 6.1.

3.3 Loop filter

The loop filter provides frequency-dependent gain and phase advance that can be tuned to optimize closed loop

[6] RAM can be due to polarization drift upstream of the EOM and etalon effects due to interference of stray reflections along the beam path [8, 33].

performance (see Sect. 2.2). We focus on analog PID loop filters which have several salient properties.

- adjustable fast-branch $\hat{K}_{\text{fast}}$ parameters: K_P, f_I, f_D as shown in Eq. (6)
- adjustable slow-branch $\hat{K}_{\text{slow}}$ parameter: f_I^{slow}, $\hat{K}_{\text{slow}} = -jf_I^{\text{slow}}/f$
- adjustable input offset m_6^{DC}
- propagation delay
- low-frequency integral gain limit

As discussed in the introduction, the widely-used PID loop filter provides 3 free parameters: f_I, f_D, and K_P [5].[7] The corresponding transfer function is Eq. (6). The input offset m_6^{DC} can compensate for the error signal offset. The propagation delay of a good analog PID can be as low as 10 ns [64, 65]. This corresponds to less than −36° at 10 MHz.

Although $|\hat{\alpha}| \to \infty$ seems like it might be optimal, it is common to limit the integral gain at low frequencies. When initially engaging the lock, the error signal may be far from zero due to laser noise and large I-gain near DC can drive the feedback to saturation. This can be mitigated by first establishing an initial lock using the fast branch and later slow branch. Note that even when system performance is shot-noise limited, high-gain at low frequency is not needed [1, 2, 51, 66].

Digital loop filters based on field-programmable gate array (FPGA) have been developed and successfully applied in AMO experiments including laser locking [67–72]. They can provide more diverse transfer functions with features like providing more than 90° lead or lag, multiple inputs and outputs, auto-relock, integrator hold, and system discovery. However, their delay is typically > 200 ns which ultimately limits the phase lead and they are limited by high input noise $50 - 100\,\text{nV}/\sqrt{\text{Hz}}$ at 1 kHz [67, 68]. Both are approximately 20-times higher than those for a high-performance analog loop filter[8] In the case of laser linewidth reduction, maximizing f_{UG} is the highest priority and analog feedback is best for the fast branch. For the slow-branch $\hat{K}_{\text{slow}}$, delay is not a problem and a digital loop filter may be a good choice [9, 42]. Additional resources for loop filter design include Ref. [5, 7, 8].

[7] Note that some loop filters have adjustable parameters K_P, K_I, K_D where the transfer function is $\hat{K} = K_P - jK_I/f + jK_D f$. This is a poor choice since the pole is $f_I = K_I/K_P$ and the zero is $f_D = K_P/K_D$ so the they can't be set independent of K_P. Loop filters like this cost extra tuning work in optimizations.

[8] Commercial examples include the Toptica FALCpro and Vescent D2-125 [65].

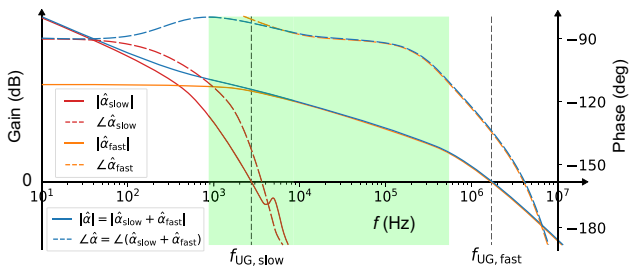

Fig. 3 Sample Bode plots of the transfer function of the fast ($\hat{\alpha}_{\text{fast}}$) and slow branches ($\hat{\alpha}_{\text{slow}}$). $f_{\text{UG,slow}}$ and $f_{\text{UG,fast}}$ are UG points for the slow- and fast-branch feedback. Our recommendation is that the cavity pole $\delta\nu_c/2$ lies in the green-shaded region

3.4 Cavity selection

Finally we discuss is the linewidth $\delta\nu_c$ choice of the reference cavity. Industry-standard reference cavities have an FSR of 1.5 GHz leaving finesse (linewidth $\delta\nu_c$) as the primary free parameter. Our recommendation balances the trade-offs discussed below (Fig. 3).

A low-noise lock favors small $\delta\nu_c$. The PSD of Eq. (17) is

$$S_{y1} = \frac{1}{|1+\hat{\alpha}|^2} S_{n1} + \frac{|\hat{\alpha}|^2}{|1+\hat{\alpha}|^2} \frac{1}{k_e^2 |C|^2} S_{n4} \tag{18}$$

Since $1/(k_e^2|C|^2) \propto \delta\nu_c^2 + 4f^2$, smaller $\delta\nu_c$ gives less sensitivity to discriminator noise n_4. Note that choosing $\delta\nu_c$ too small can make cavity alignment hard because of low transmission and make locking hard since the laser is commonly servo'd manually to $y_1 \in (-\delta\nu_c/2, \delta\nu_c/2)$ before activating the lock.

The optimal choice of the cavity pole $\delta\nu_c/2$ to maximize f_{UG} is $\delta\nu_c/2 > \sqrt{10} f_{\text{UG,fast}}$, as indicated by the phase response of a low-pass filter (see Fig. 1d). However, as shown in Eq. (18), a small $\delta\nu_c$ suppresses discriminator noise. Therefore, the sub-optimal but noise-favorable choice is $\delta\nu_c/2 < f_{\text{UG,fast}}/\sqrt{10}$. Avoid overlap of $\delta\nu_c/2$ with $f_{\text{UG,fast}}$, else the phase margin is more sensitive to laser power or RAM drift because of steeper $d\angle\hat{\alpha}/df$ near $f_{\text{UG,fast}}$. If fast branch cannot fully suppress slow branch servo bump, less $\angle\hat{C}$ when $\delta\nu_c/2 > \sqrt{10} f_{\text{UG,slow}}$ is helpful. For a typical ECDL we have $f_{\text{UG,fast}} \sim 1 - 2$ MHz and $f_{\text{UG,slow}} \sim 1 - 10$ kHz, for which the recommended range of $\delta\nu_c$ is the green-shaded range in Fig. 3.

State-of-the-art mirror coating can achieve a finesse of 10^6 [13, 16, 73, 74]. Given a cavity length of 10 to 50 mm [16, 17, 27, 54, 75], a practical lower bound on linewidth is around 1 kHz.

4 Closed-loop optimization

In an all-electronic system, a vector network analyzer (VNA) can be used to probe each system component separately to determine its transfer function and noise. The present context is a mixed optical-electronic system so we in addition need an optical frequency discriminator (OFD). Required properties of this OFD include sensitivity at the wavelength of interest, a bandwidth well above the target f_{UG} and sensitivity to small frequency deviations (and therefore high stability over time). We also want a frequency-agile optical source such as a tunable laser or EOM. However, in many labs the only suitable OFD available is the PDH discriminator $\hat{H}_{v_c}$ we want to optimize! Further, measuring the PDH OFD transfer function by open-loop techniques is impractical since the reference cavity linewidth is typically small relative to the free-running laser linewidth. In this chicken-and-egg situation the most expedient solution is to measure what we can using open loop techniques, then rely on closed-loop measurements to estimate the OFD and laser transfer functions. The closed loop probe relies on a VNA to inject stimulus at summing points m_k while measuring electrical loop signals y_k which are related as

$$\begin{pmatrix} y_5 \\ y_6 \\ y_8 \end{pmatrix} = \frac{1}{1+\hat{\alpha}} \begin{pmatrix} \hat{H}_{v_c} & \hat{\alpha} & \frac{\hat{\alpha}_{\mathrm{fast}}}{\hat{K}_{\mathrm{fast}}} \\ -\hat{H}_{v_c} & 1 & -\frac{\hat{\alpha}_{\mathrm{fast}}}{\hat{K}_{\mathrm{fast}}} \\ -\frac{\hat{\alpha}_{\mathrm{fast}}}{\hat{G}_{\mathrm{fast}}} & \hat{K}_{\mathrm{fast}} & 1+\hat{\alpha}_{\mathrm{slow}} \end{pmatrix} \begin{pmatrix} m_2 \\ m_6 \\ m_8 \end{pmatrix} \tag{19}$$

See signals y_k and modulation m_k in Fig. 5. Then we are in a position to optimize the overall loop.

4.1 System optimization workflow

We use the following workflow to tune loop filter parameters and check for several misconfiguration errors. It consists of four steps: prepare, measure, optimize and check.

prepare:

1. Measure the transfer function of each loop component.
2. Sweep the laser frequency across the cavity resonance and observe the error signal $\tilde{y}_5$ line shape on an oscilloscope (Fig. 2). Make the error signal symmetric about $\tilde{y}_5 = 0$ by adjusting the phase ϕ_o of the RF source (Fig. 5a).
3. Sweep across the cavity resonance and observe the fast loop filter output $\tilde{y}_8$ on an oscilloscope. Adjust the input offset m_6^{DC} to make $\tilde{y}_8$ symmetric about zero.
4. To null the slow loop offset do as follows. Far detune the laser from resonance. Turn on the slow loop filter and observe the rate at which output $\tilde{y}_7$ rails. Adjust the slow input offset to minimize the rate. This offset is not shown in Fig. 5.
5. To initialize the loop filter: minimize f_I and disable f_D.
6. Close the loop and obtain a weak lock starting with the fast branch of the loop filter. Increase K_P until the loop oscillates then reduce K_P by 50%. Next, add f_I until the loop oscillates then reduce f_I by 50%. Finally add K_P back a little. Signals $\tilde{y}_5$ and $\tilde{y}_8$ show periodic waveform on the oscilloscope when the loop oscillates.
7. Next enable the slow integrator $\hat{K}_{\mathrm{slow}}$. Increase f_I^{slow} until the loop oscillates. Then reduce it until oscillation disappears.

measure:

1. Measure y_5/m_6 by connecting a VNA as shown in Fig. 5a. Program the VNA to apply stimulus at m_6 and record the response at y_5 for frequencies up to 10 MHz. The injected amplitude should be low enough to keep $\tilde{y}_5$ in the linear region; vary the amplitude of m_6 with frequency as needed. Make a Bode plot of y_5/m_6.
2. Take note of the frequency f_{180}^{CL} which is where $\angle(y_5/m_6) = -180°$.[9]
3. Measure $\tilde{y}_5$ on an oscilloscope and note its RMS value $\tilde{y}_5^{\mathrm{RMS}}$ which is proportional to laser frequency fluctuation $\tilde{y}_1^{\mathrm{RMS}}$.[10] Equivalently, you can avoid $1/f$ noise in $\tilde{y}_5$ by using a spectrum analyzer to measure S_{y4}.

optimize:

First, check if there is excess low-frequency noise; we want $|y_5/m_6| \approx 1$ and $\angle y_5/m_6 \approx 0°$ for $f < f_{180}^{\mathrm{CL}}/10$ (see Fig. 4). If not, reduce fast-branch high-pass $f_{\mathrm{HP,fast}}$. If the problem persists, reduce slow-branch f_I^{slow}.

Next, try to increase f_{180}^{CL}.

1. Enable and reduce f_D until oscillation, then raise it by 50%. Increase K_P until oscillation, then reduce it by 50%. Increase f_I until oscillation, then reduce it by 50%. Then, reduce f_D until oscillation, then raise it by 50%. Loop over adjustments to K_P, f_I, and f_D repeatedly until no further improvements can be made. Finally, slightly raise K_P again.

[9] Observe that $f_{180}^{\mathrm{CL}} = f_{180}$. This is because $\hat{\alpha}(f_{180})$ is real and $-1 < \hat{\alpha}(f_{180}) < 0$ when the loop is stable, so too $\hat{\alpha}/(1+\hat{\alpha})$ is real and negative. Thus $f_{180}^{\mathrm{CL}} = f_{180}$. Checking f_{180}^{CL} is quicker. Improving f_{180} is equivalent to improve f_{UG}.

[10] Note that $\tilde{y}_5^{\mathrm{RMS}} = \sqrt{\int_0^\infty S_{y5} df} = \sqrt{\int_0^\infty \left|\hat{H}_{v_c}\right|^2 S_{y1} df} = \left|\hat{H}_{v_c}(\xi)\right|^2 \sqrt{\int_0^\infty S_{y1} df} = \left|\hat{H}_{v_c}(\xi)\right|^2 \tilde{y}_1^{\mathrm{RMS}}$, where ξ is a finite frequency.

2. While observing $\tilde{y}_5^{\mathrm{RMS}}$, minimize the observable while fine tuning K_P. Alternately, you may minimize $\sqrt{\int_{a_-}^{a_+} S_{y4} df}$, where $a_\pm = \Omega/2\pi \pm 5\,\mathrm{MHz}$[11]

check:

Start by calculating the open-loop transfer function $\hat{\alpha}$ from the VNA measurement.

$$\frac{y_5}{m_6} = \frac{\hat{\alpha}}{1+\hat{\alpha}} \implies \hat{\alpha} = \frac{y_5/m_6}{1 - y_5/m_6} \tag{20}$$

Generate a Bode plot of $\hat{\alpha}$ and locate f_{UG} and ϕ_m. Then check the following.

1. If f_{UG} is not as high as you hoped, revisit Sect. 3 and use components with less phase lag. Adjusting the loop filter won't help.
2. If $\tilde{y_5}^{\mathrm{RMS}}$ (or S_{y4}) is satisfactory but $\phi_m < 30°$, you can increase ϕ_m at the expense of degraded $\tilde{y}_5$ RMS by reducing K_P. Increased ϕ_m improves loop stability.
3. We expect that $\angle\hat{\alpha}$ is the sum of the phase shift from the individual components: $\angle\hat{K}_{\mathrm{fast}} + \angle\hat{G}_{\mathrm{fast}} + \angle\hat{C} + \angle\hat{D} + \angle\hat{P} + \angle\hat{T}$. If excess phase lag is observed, dig to find the source.

4.2 Example optimization

In this section we illustrate application of the system optimization workflow (Sect. 4.1) to improve $\hat{\alpha}$ for a representative laser system. There are three system configurations (Table 1) where the loop is diagnosed and incrementally improved. The optical and electronic elements of the PDH setup are shown in Fig. 5.

4.2.1 Configuration 1

The initial, unoptimized configuration is as follows. The laser is a 1650 nm Littrow ECDL with a 70 dB optical isolator. We observe a free-running frequency fluctuation of ~ 200 kHz over a 10 ms integration window by monitoring side-of-fringe transmission from a test cavity with a full-width at half-max (FWHM) linewidth 4.2 MHz (Thorlabs SA200-12B [65]). The laser controller has external inputs to modulate the PZT voltage (slow branch) and the laser diode current (fast branch). The PZT actuator has a lowest mechanical resonance at 6 kHz. Using the technique in Appendix 6.3 we observe that current modulation exhibits a −52° phase shift at 1 MHz.

Sidebands are applied to the laser light using a fiber EOM (iXblue MPZ-LN-10 [65]) driven at $\Omega/2\pi = 20$ MHz with

[11] Integrate over a fixed range larger than larger f_{180}^{CL}, here we use 5 MHz.

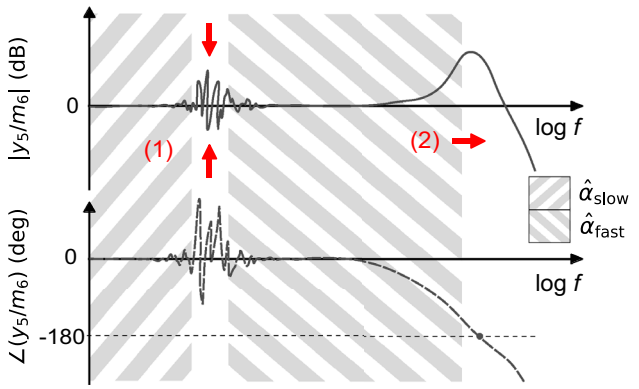

Fig. 4 A sample closed-loop transfer function y_5/m_6 for an incorrectly tuned system. We want to adjust the loop parameters to (1) obtain $y_5/m_6 \approx 1$ for $f < f_{180}^{\mathrm{CL}}/10$. (2) maximize f_{180}^{CL}. The gray-white striped regions show the ranges in which the slow and fast feedback attenuate noise. We aspire to eliminate the white gap between them

voltage $\beta/\pi \cdot V_\pi \approx 1.5$ V for $\beta = 1.082$. The thermally and acoustically isolated reference cavity (Stable Laser Systems [65, 76]) is made of ultra-low expansion glass (ULE). The cavity has planar and concave ($R = -50$ cm) mirrors separated by 10 cm. It is temperature-stabilized at 24.7 °C where the linear thermal expansion coefficient is zero. The cavity FSR is 1.5 GHz, its FWHM as measured by ring down is $\delta\nu_c = 45.7$ kHz (see Appendix 6.2) and its finesse at 1650 nm is $\mathscr{F} = \nu_{\mathrm{FSR}}/\delta\nu_c \approx 33,000$. The laser was consistently locked to the same cavity transmission feature at $\nu_c = 181.65917$ THz using a Michelson interferometer-based wave meter (Bristol 228A [65]) to disambiguate cavity transmission features.

The PD for cavity-reflected light (PD1 in Fig. 5a) is a reverse-biased InGaAs diode (Thorlabs PDA10D2 [65]) with an NEP = 39 pW/$\sqrt{\mathrm{Hz}}$, a bandwidth $f_{\mathrm{PD}} = 20$ MHz, and $\angle\hat{P} = -6.2°$ at 1 MHz. An optical power of 850 µW incident on the cavity results in 650 µW at PD1. The SNR for PD1 is greater than 2700. We use a Level 7 mixer (MiniCircuits ZAD-1-1+ [65]). Using the technique in Appendix 6.4 we determine that the mixer adds a phase lag of −1° at 1 MHz. A dual-channel RF signal generator (Rigol DG822 [65]) generates Ω with a phase offset for the tone sent to the mixer LO port. The low-pass (LP) (Minicircuits BLP−10.7+ [65]) is an 8th order modified Butterworth-type filter with a corner frequency of 14 MHz and a −22° phase lag at 1 MHz; the LP provides −34 dB suppression at Ω. A high-speed analog loop filter was used with < 45° electronic phase delay at 10 MHz (Toptica FALC 110 [65, 77]).

We used a vector network analyzer (VNA, OMICRON Lab Bode 100 [65]) for transfer function measurements and a spectrum analyzer (Rohde & Schwarz FSV40-N [65]) to measure the noise spectrum.

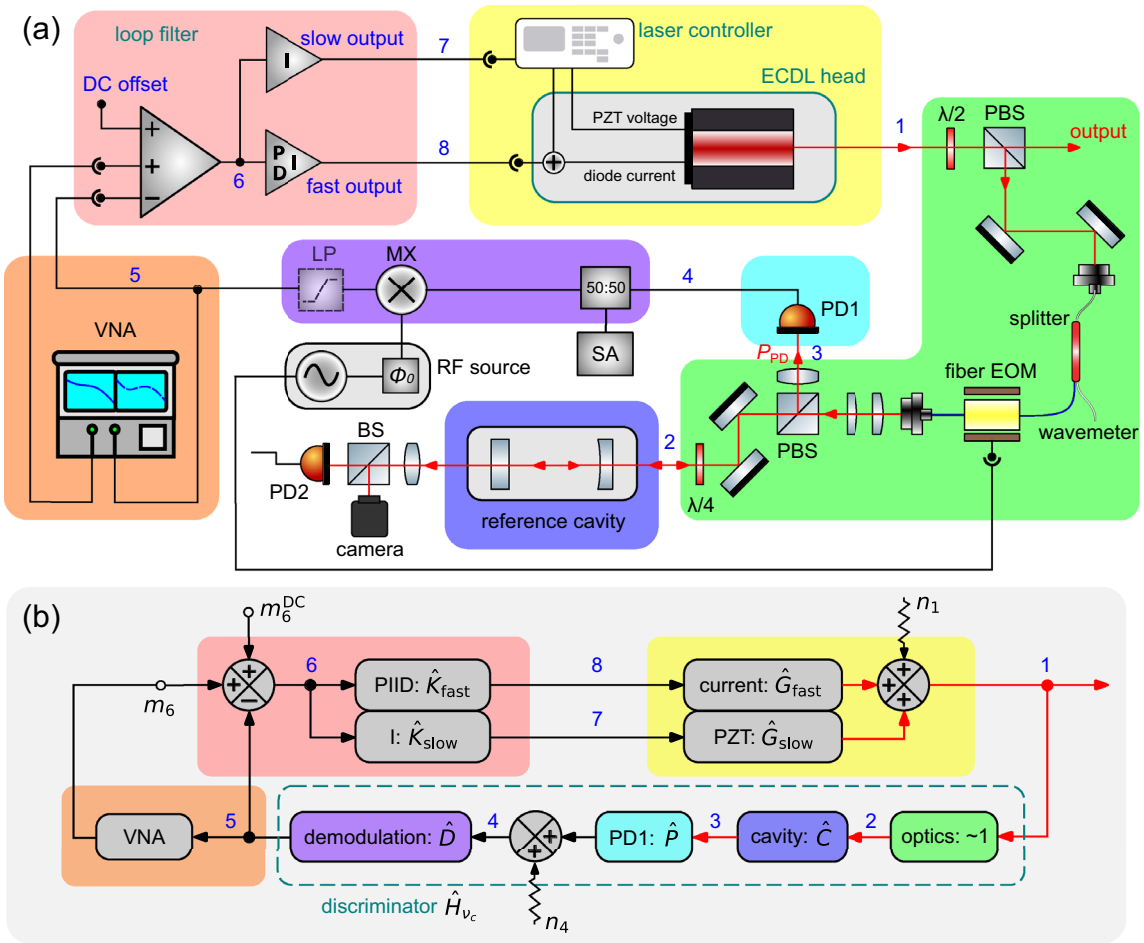

Fig. 5 **a** A schematic for the components in a PDH laser frequency stabilization setup. Positions within the loop are labeled with number k in blue. Loop signals y_k is defined to include modulation m_k or noise n_k at summing points (not drawn for m_2 and m_8). Black (red) labels denote electrical (optical) signals. Light from an ECDL acquires sidebands at $\pm\Omega$ from a fiber EOM, is reflected off a reference cavity and incident on a photodetector (PD1). The PD1 signal is demodulated to generate error signal y_5. In closed-loop analysis, a VNA injects stimulus at position 6. Outputs of the loop filter are sent to the laser actuators, completing the loop. A camera and PD2 are used to check cavity transmission and alignment. A spectrum analyzer (SA) is at position 4. **b** A block diagram of the feedback loop in **a**. Transfer functions for each component are denoted by capital letters (eg $\hat{C}$). A dashed line encloses the optical frequency discriminator $\hat{H}_{v_c} = \hat{D}\hat{P}k_e\hat{C}$. Free-running laser noise n_1 and discriminator noise n_4 (including the noises in PD, RAM noise, cavity drifts, etc.) are summed into the loop as indicated

4.2.2 Configuration 2

We were not satisfied with the low $f_{UG} \approx 0.5$ MHz for configuration 1. We found several components could be optimized to reduce their phase lags. The following changes were made for configuration 2.

The PD1 was changed to PDA05CF2 [65] ($f_{PD} = 150$ MHz) which has lower noise NEP $= 6.3\,\text{pW}/\sqrt{\text{Hz}}$ at 1650 nm and smaller phase lag $\angle\hat{P} = -1.3°$ at 1 MHz. The optical power P_{PD} was reduced from 650 µW to 430 µW to accommodate increased PD efficiency, and provides a better SNR≈ 6800. The loop length was reduced by 6.8 m. More phase lead was added by increasing the D term in the loop filter. In total, we get +26.6° phase lead at 1 MHz relative to configuration 1.

4.2.3 Configuration 3

We found the discrete low-pass in the demodulation circuit significantly contributed to phase lag. Removing it results in reduced SNR, but this is acceptable for us. Instead, we relied on the internal low-pass behavior of the loop filter. We get +23.5° phase lead at 1 MHz relative to configuration 2. The bulk of the remaining phase lag at 1 MHz is due to laser diode fast current modulation path. Now we found no optimizations for our setup using the workflow.

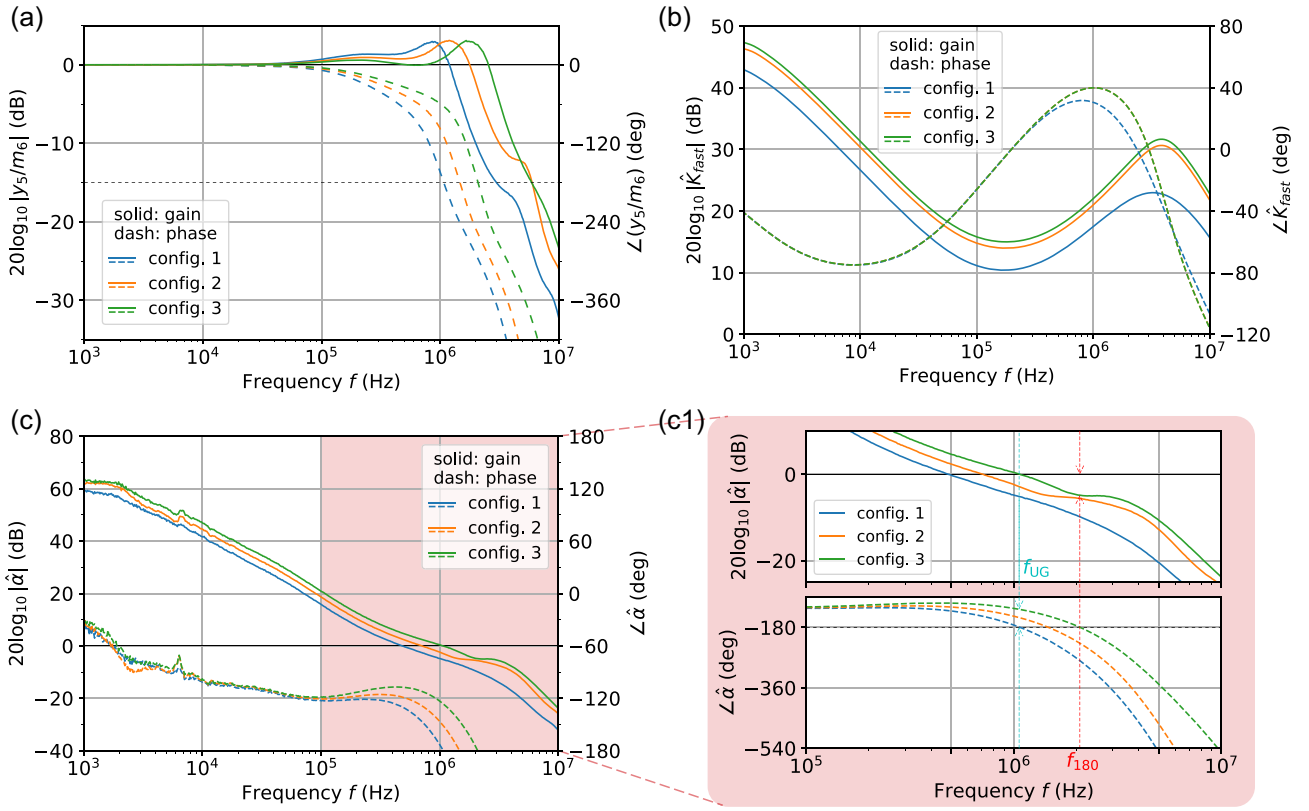

Fig. 6 Here we show performance in configuration 1, 2, and 3. **a** Bode plots of closed-loop transfer functions y_5/m_6 for the three configurations. The VNA resolution bandwidth is 10 Hz. **b** Bode plots of the fast-branch loop filter $\hat{K}_{\text{fast}}$. **c** Bode plots of open-loop transfer function $\hat{\alpha}$ calculated from $\frac{y_5/m_6}{1-y_5/m_6}$. As expected the slope of $|\hat{\alpha}|$ is approximately -20 dB/decade. (c1) Zoom-in of the red-shaded area of plot **c**. For configuration 3, we call out the UG point f_{UG} and phase crossover point f_{180}

4.2.4 Optimization results

Table 1 summarizes the performance for each configuration. We see improvements in f_{UG} while ϕ_m remains in the recommended range. In Table 2 we show that from measurement of the individual transfer functions, we can account for all phase delays in the loop. This gives us confidence that we understand the origin of phase lags in our setup and have addressed them during optimization.

We also measured the noise spectra $S_{y4}(f)$ of cavity-reflected signal y_4 by a spectrum analyzer (Fig. 7a). Servo bumps f_{bump} are summarized in Table 1. Improving f_{UG} pushes servo bumps to higher frequencies and enhances the noise suppression for all $f < f_{\text{bump}}$.

The single-sided laser frequency PSD S_{y1} is plotted in Fig. 7b. This quantity is calculated by shifting S_{y4} by $-\Omega/2\pi$ and dividing by $|\hat{H}_{v_c}/\hat{D}|^2$. The error signal slope was measured to be $k_e = 2.69$ mV/kHz. We use the $\hat{D}$ and $\hat{P}$ from Appendix 6.4.

We would like to compare S_{y1} for the free-running and for the locked laser, however we can't measure the free-running PSD due to the narrow linewidth of our reference cavity. Instead we model the free-running behavior by Eq. (10). Since above f_{UG} there is no noise suppression even when feedback is active, the value of h_0 can be determined from the closed-loop response: $h_0 = S_{y_1}(5\text{ MHz}) = 2\times10^3\text{ Hz}^2/\text{Hz}$. We set $h_{-1} = 5\times10^8\text{ Hz}^2$ which is close to the values from reported frequency noise spectrum of Toptica ECDLs [78–81]. The shaded red area contributes to a linewidth of ~ 150 kHz according to the β-separation line theory [47]. In comparison with the free-running laser performance it's clear configuration 2 and 3 have substantially reduced laser linewidth.

We are satisfied with our laser performance after two iterations of optimization where we pushed f_{UG} from 0.49 to 1.06 MHz with the recommended phase margin and showed linewidth narrowing based on an analysis of the PSD of S_{y4}. We also systematically checked that the sum of phase shifts from all individual components, measured in open loop, was in a good agreement with $\angle\hat{\alpha}$, measured in closed loop. So we are confident in our understanding

Table 1 A summary of key metrics for each configuration

Configuration	UG point f_{UG} (MHz)	Phase margin ϕ_m (deg)	Servo bump f_{bump} (MHz)
1	0.49	50	0.91
2	0.71	51	1.32
3	1.06	54	1.94

Table 2 Tabulation of the configuration 3 phase shifts at $f_{\mathrm{UG}} = 1.06$ MHz

Component	Phase shifts (deg) at $f_{\mathrm{UG}} = 1.06$ MHz	Source
$\angle\hat{K}_{\mathrm{fast}}$	+40	From Fig. 6b
$\angle\hat{G}_{\mathrm{fast}}$	−52	See Appendix 6.3
$\angle\hat{C}$	−89	Calculated from Eq. (14)[a]
$\angle(\hat{D}\hat{P})$	−9	See Appendix 6.4
$\angle\hat{T}$	−15	$-360°f_{\mathrm{UG}}\tau_l$ [b]
$\angle\hat{\alpha}$	−126	From Fig. 6(c1)

The sum of the phase shifts from individual components differs from the measured $\angle\hat{\alpha}$ by less than 5°. Since $f_{\mathrm{UG}} = 1.06$ MHz, $\hat{K}_{\mathrm{slow}}(f_{\mathrm{UG}}) \approx 0$ and $\hat{G}_{\mathrm{slow}}(f_{\mathrm{UG}}) \approx 0$, we ignore $\hat{\alpha}_{\mathrm{slow}}(f_{\mathrm{UG}})$

Remarks: a $\delta\nu_c = 45.7$ kHz, see the ring-down measurement in Appendix 6.2

b Here τ_l is the delay due to signal propagation thru 2.1 m free space, 4.9 m fiber, and 1.7 m coaxial cable. Dispersion in the fiber is negligible for our monochromatic continuous light

of the sources of phase lag in our system. More detailed characterization of the stability of our locked laser could be obtained using the delayed self-heterodyne technique or beating with self-referenced optical frequency comb.

5 Summary

We hope this tutorial proves useful to practitioners learning to implement laser linewidth narrowing using the PDH technique. Relative to what's been published before our treatment pulls together ideas on component optimization and VNA informed loop filter optimization.

Appendix

6.1 Phase shift in lock-in detection

We derive the phase shift in demodulated error signal $\tilde{y}_5$ due to the PD between the modulation and demodulation. The light reflected from cavity generates a signal $\tilde{y}_4$ on the PD. We check $\tilde{y}_4$ at Fourier frequency f (2Ω terms are removed by the low-pass filter),

$$\tilde{y}_4(t) = V_- \cos\left[(\Omega - 2\pi f)t + \phi_-\right] + V_+ \cos\left[(\Omega + 2\pi f)t + \phi_+\right]$$

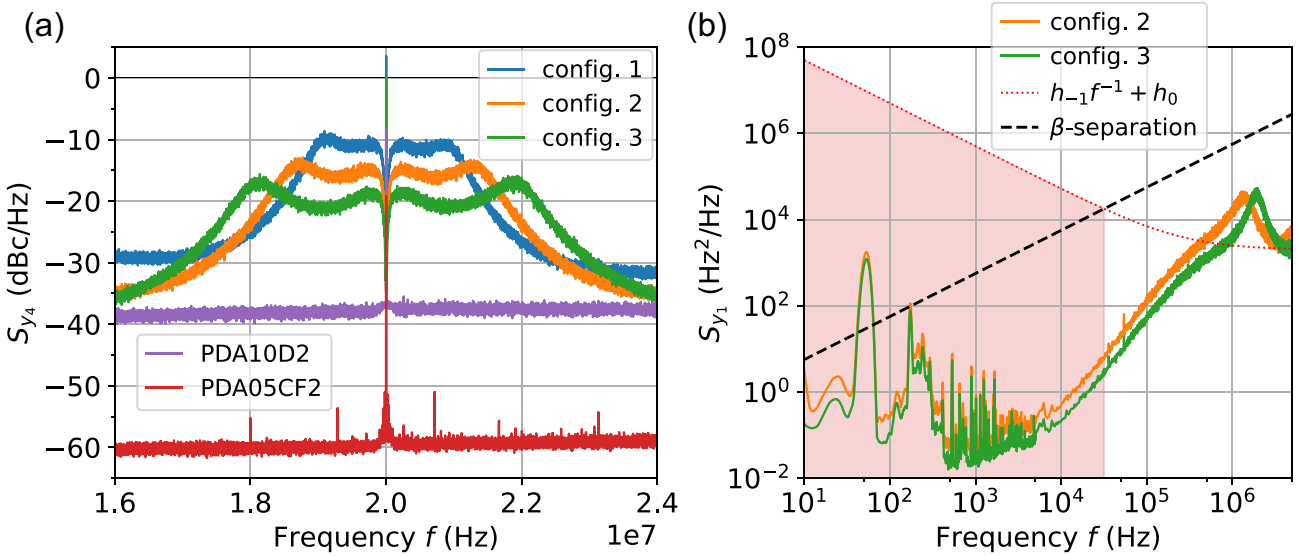

Fig. 7 **a** The power spectral density S_{y4} of the three configurations and the two PDs. The PSD are normalized to configuration 3 and have a 1 kHz resolution bandwidth. Photodetector baselines are measured with the laser blocked; the 20 MHz carrier leakage is due to imperfect mixer LO-RF isolation. **b** Here we show evidence of linewidth narrowing. We plot the PSD S_{y1} of the configuration 2 and 3 (solid lines) while locked and a model for the free-running laser (dotted red line). We also plot the β-separation line (dashed black). The PDH-locked S_{y1} are calculated from measured S_{y4} with a 10 Hz resolution bandwidth and the PD noise baseline is subtracted

$V_\pm$ and $\phi_\pm$ represent different gains and phase shifts at $\Omega/2\pi \pm f$ added by the PD ($\phi = \angle\hat{L}_{\rm PD}$, $\hat{L}_{\rm PD}$ is the PD transfer function without lock-in). $\tilde{y}_4$ is then mixed with a LO signal with a tunable demodulation phase ϕ_0 to generate the error signal $\tilde{y}_5$,

$$\begin{aligned}\tilde{y}_5 &\propto \tilde{y}_4(t) V_{\rm LO} \cos\left(\Omega t + \phi_0\right) \\ &\propto \frac{1}{2} V_{\rm LO} \sqrt{A^2 + B^2} \cos\left(2\pi f t + \varphi\right)\end{aligned}$$

$$\begin{aligned}A &:= V_- \cos\left(\phi_0 - \phi_-\right) + V_+ \cos\left(\phi_+ - \phi_0\right) \\ B &:= V_- \sin\left(\phi_0 - \phi_-\right) + V_+ \sin\left(\phi_+ - \phi_0\right)\end{aligned}$$

$$\tan\varphi = \frac{B}{A} = \frac{V_- \sin\left(\phi_0 - \phi_-\right) + V_+ \sin\left(\phi_+ - \phi_0\right)}{V_- \cos\left(\phi_0 - \phi_-\right) + V_+ \cos\left(\phi_+ - \phi_0\right)}$$

A single ϕ_0 cannot compensate both $\phi_\pm(\Omega/2\pi \pm f)$. Because the PD bandwidth is usually much higher than $\Omega/2\pi$, phase ϕ is approximately linear, so choose $\phi_0 = \phi(\Omega/2\pi) \approx \frac{1}{2}(\phi_- + \phi_+)$, we get

$$\varphi(f) = \left[\phi(\Omega/2\pi + f) - \phi(\Omega/2\pi - f)\right]/2 \tag{21}$$

The gain of PD has been absorbed in the definition of slope k_e, so we define PD transfer function in lock-in detection as $\hat{P}(f) = e^{i\varphi(f)}$.

6.2 Cavity ring-down measurement

The reference cavity linewidth $\delta\nu_c$ was determined from a ring-down experiment. The PD2 in Fig. 5 measured the power transmitted by the cavity. A wideband EOM amplitude modulator (AM-EOM, iXblue MXER-LN-10) was inserted after the optical splitter. The AM-EOM extinction was small but sufficient for this measurement. A ring-down measurement cycle consisted of the steps: lock the laser to the cavity, attenuate the laser light with the AM-EOM and record the decaying PD2 signal. The ring-down trace in Fig. 8 is an average of 256 ring-down repetitions. An exponential fit to this average yields $\delta\nu_c = (45.7 \pm 0.2)$ kHz.

6.3 Frequency modulation via diode current

We measured the transfer function of the ECDL fast branch ($\hat{G}_{\rm fast}$) using a PDH discriminator (Fig. 9a). The discriminator configuration is similar to Fig. 5a, except that the SLS optical cavity was replaced by a Fabry-Perot interferometer (FPI, Thorlabs SA200-12B [65]) with linewidth $\delta\nu_{\rm FPI} = 5.4$ MHz.[12] The FPI linewidth is broad relative to the free-running laser frequency instability over the duration

[12] from an independent linewidth measurement.

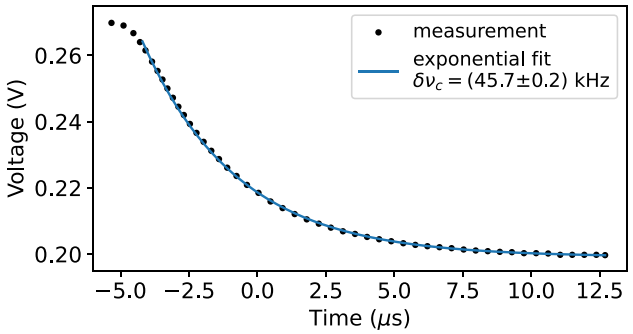

Fig. 8 The reference cavity linewidth $\delta\nu_c$ is determined by a ring-down measurement as described in the text. Initial transient behavior is excluded from the fit

of our measurement. The transfer function was measured by tuning the laser on resonance and monitoring the PDH error signal while modulating the diode current using a VNA. The laser transfer function $\hat{G}_{\rm fast}$ was determined after numerically accounting for shifts due to propagation delay and other components in the PDH discriminator (Fig. 9b). The phase shift at $f_{\rm UG} = 1.06$ MHz is $-51.9°$ and dominates our accounting of the overall loop phase delay (Table 2). In addition to the possible phase lag from the laser diode driver circuit [46], we suspect the large lag at 1 MHz could be due to sub-optimal alignment of the optical feedback to the diode [7] or laser diode thermal effects [7, 8]. Reference [39] offers an excellent discussion on discussion on the phase lag introduced by laser diodes.

Note that the PDH error signal transfer function is a 1st-order low-pass (Eq. 14). However, the cavity transmission response to laser frequency modulation is a 2nd-order low-pass [39, 82, 83], making it slower and more challenging to analyze.

6.4 PDH demodulation electronics

In this appendix we measure the transfer function of the PDH demodulation electronics $\hat{D}\hat{P}$ consisting of PD $\hat{P}$ and mixer plus low-pass $\hat{D}$. Recall the contribution of the quantity $\hat{D}\hat{P}$ to the overall PDH discriminator transfer function in Eq. (16). The device under test is the enclosed by the dashed cyan line in Fig. 10a.

Modulation in laser light is applied by the fast AM-EOM. An extra mixer MX1 up-converts VNA modulation to $\Omega/2\pi$. We independently check mixer transfer functions by cascading two identical mixers (one up-convert, the other down-convert). After compensating the lag of MX1 and propagation delay in fiber, we get $\hat{D}\hat{P}$. In Fig. 10b, the phase lag traces of 50:50 RF splitter, low-pass filter and cable delay are measured individually by VNA. $\angle\hat{L}_{\rm PD}$ of PD (PDA05CF2) is measured by VNA modulating the AM-EOM and then

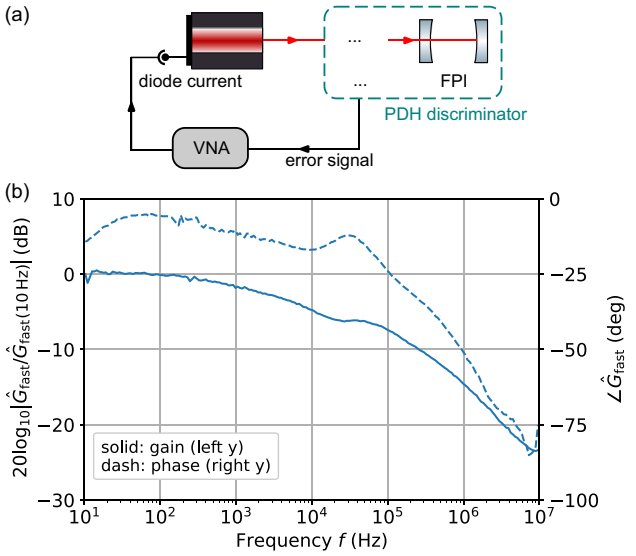

Fig. 9 Setup **a** was used to measure the transfer function $\hat{G}_{\text{fast}}$ of the laser fast branch actuator. **b** A Bode plot of the relative gain and phase for the fast branch frequency modulation via diode current

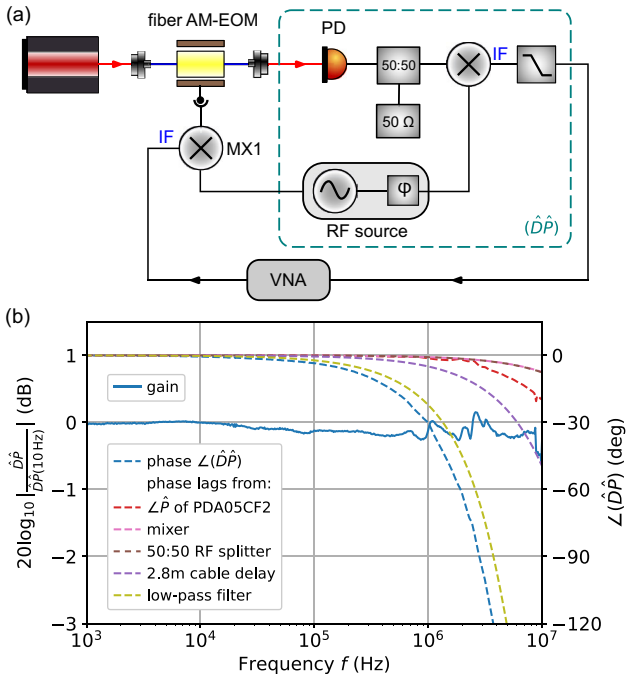

Fig. 10 **a** The setup to measure the transfer function $\hat{D}\hat{P}$ (components in the cyan dash box). AM-EOM is the wideband EOM amplitude modulator. An extra mixer MX1 up-converts VNA modulation to $\Omega/2\pi$ frequency. The transfer function of MX1 is measured separately to compensate the measurement in **a**. **b** Bode plots of $\hat{D}\hat{P}$ (blue solid and dash lines) and the phase lags from the components in $\hat{D}\hat{P}$ (dash lines in other colors). Measurements of individual components are elaborated in Appendix 6.4.

$\angle\hat{P}$ is calculated from Eq. (13). At $f_{\text{UG}} = 1.06$ MHz of the configuration 3, the sum of individual lags are $-31.9°$, which matches well with $\angle(\hat{D}\hat{P}) = -32.8°$. This check further confirms that our transfer function model in Appendix 6.1 works and there is no unknown phase lag in the lock-in detection.

Acknowledgements We thank Dr. Alessandro Restelli at the University of Maryland, Dr. David Nadlinger at the University of Oxford, and Dr. Chin-wen Chou at the National Institute of Standards and Technology for their helpful discussion. This work was funded by Army Research Laboratory (Sponsor Award Number: W911NF2420107).

Author Contributions W.W. developed the conceptual framework and methodology for the control theory tutorial, component selection, and closed-loop optimization sections. W.W. also conducted the experimental investigation and validation presented in the manuscript, including data acquisition, processing, and visualization. S.S. developed the conceptualization and methodology for the closed-loop optimization section and shared the early-stage investigation. J.B. contributed to the conceptualization of the control theory tutorial and component selection sections, provided supervision, managed the project administration, and secured resources and funding. W.W. and J.B. wrote the primary manuscript, with contributions from S.S. All authors reviewed the final manuscript.

Data availability The data that support the findings of this study are available from the corresponding author upon reasonable request.

References

1. E.D. Black, Am. J. Phys. **69**, 79 (2000). https://doi.org/10.1119/1.1286663
2. T. Day, E. Gustafson, R. Byer, IEEE J. Quantum Electron. **28**, 1106 (1992). https://doi.org/10.1109/3.135234
3. J.I. Thorpe, K. Numata, J. Livas, Opt. Express **16**, 15980 (2008). https://doi.org/10.1364/OE.16.015980
4. C. Reinhardt, T. Müller, J.C. Sankey, Opt. Express **25**, 1582 (2017). https://doi.org/10.1364/OE.25.001582
5. J. Bechhoefer, Rev. Mod. Phys. **77**, 783 (2005). https://doi.org/10.1103/RevModPhys.77.783
6. K. Ogata, *Modern Control Engineering*, vol. 5, 5th edn. (Pearson Education, London, 2010)
7. J.L. Hall, M.S. Taubman, J. Ye, *Handbook of Optics*, vol. IV, v14 edn. (McGraw-Hill Professional, New York, 1999), p.24
8. R.W. Fox, C.W. Oates, L.W. Hollberg, *Stabilizing Diode Lasers to High-Finesse Cavities*, vol. 46 (National Institute of Standards and Technology, Boulder, 2003)

9. W. Nagourney, *Quantum Electronics for Atomic Physics and Telecommunication*, 2nd edn. (Oxford University Press, Oxford, 2014). https://doi.org/10.1093/acprof:oso/9780199665488.001.0001
10. R.W.P. Drever, J.L. Hall, F.V. Kowalski, J. Hough, G.M. Ford, A.J. Munley, H. Ward, Appl. Phys. B **31**, 97 (1983). https://doi.org/10.1007/BF00702605
11. B.C. Young, F.C. Cruz, W.M. Itano, J.C. Bergquist, Phys. Rev. Lett. **82**, 3799 (1999). https://doi.org/10.1103/PhysRevLett.82.3799
12. A.D. Ludlow, X. Huang, M. Notcutt, T. Zanon-Willette, S.M. Foreman, M.M. Boyd, S. Blatt, J. Ye, Opt. Lett. **32**, 641 (2007). https://doi.org/10.1364/OL.32.000641
13. Y.N. Zhao, J. Zhang, J. Stuhler, G. Schuricht, F. Lison, Z.H. Lu, L.J. Wang, Opt. Commun. **283**, 4696 (2010). https://doi.org/10.1016/j.optcom.2010.06.079
14. Y.Y. Jiang, A.D. Ludlow, N.D. Lemke, R.W. Fox, J.A. Sherman, L.-S. Ma, C.W. Oates, Nat. Photon **5**, 158 (2011). https://doi.org/10.1038/nphoton.2010.313
15. T. Kessler, C. Hagemann, C. Grebing, T. Legero, U. Sterr, F. Riehle, M.J. Martin, L. Chen, J. Ye, Nat. Photon **6**, 687 (2012). https://doi.org/10.1038/nphoton.2012.217
16. D.G. Matei, T. Legero, S. Häfner, C. Grebing, R. Weyrich, W. Zhang, L. Sonderhouse, J.M. Robinson, J. Ye, F. Riehle, U. Sterr, Phys. Rev. Lett. **118**, 263202 (2017). https://doi.org/10.1103/PhysRevLett.118.263202
17. A.D. Ludlow, M.M. Boyd, J. Ye, E. Peik, P.O. Schmidt, Rev. Mod. Phys. **87**, 637 (2015). https://doi.org/10.1103/RevModPhys.87.637
18. N. Hinkley, J.A. Sherman, N.B. Phillips, M. Schioppo, N.D. Lemke, K. Beloy, M. Pizzocaro, C.W. Oates, A.D. Ludlow, Science **341**, 1215 (2013). https://doi.org/10.1126/science.1240420
19. E. Oelker, R.B. Hutson, C.J. Kennedy, L. Sonderhouse, T. Bothwell, A. Goban, D. Kedar, C. Sanner, J.M. Robinson, G.E. Marti, D.G. Matei, T. Legero, M. Giunta, R. Holzwarth, F. Riehle, U. Sterr, J. Ye, Nat. Photonics **13**, 714 (2019). https://doi.org/10.1038/s41566-019-0493-4
20. M. Steinel, H. Shao, M. Filzinger, B. Lipphardt, M. Brinkmann, A. Didier, T.E. Mehlstäubler, T. Lindvall, E. Peik, N. Huntemann, Phys. Rev. Lett. **131**, 083002 (2023). https://doi.org/10.1103/PhysRevLett.131.083002
21. M.E. Kim, W.F. McGrew, N.V. Nardelli, E.R. Clements, Y.S. Hassan, X. Zhang, J.L. Valencia, H. Leopardi, D.B. Hume, T.M. Fortier, A.D. Ludlow, D.R. Leibrandt, Nat. Phys. **19**, 25 (2023). https://doi.org/10.1038/s41567-022-01794-7
22. A. Aeppli, K. Kim, W. Warfield, M.S. Safronova, J. Ye, Phys. Rev. Lett. **133**, 023401 (2024). https://doi.org/10.1103/PhysRevLett.133.023401
23. C. Zhang, T. Ooi, J.S. Higgins, J.F. Doyle, L. von der Wense, K. Beeks, A. Leitner, G.A. Kazakov, P. Li, P.G. Thirolf, T. Schumm, J. Ye, Nature **633**, 63 (2024). https://doi.org/10.1038/s41586-024-07839-6
24. R.J. Rafac, B.C. Young, J.A. Beall, W.M. Itano, D.J. Wineland, J.C. Bergquist, Phys. Rev. Lett. **85**, 2462 (2000). https://doi.org/10.1103/PhysRevLett.85.2462
25. M.M. Chwalla, *Precision Spectroscopy with 40Ca+ Ions in a Paul Trap*, Ph.D. thesis, school University of Innsbruck (2009)
26. A. Kleczewski, M.R. Hoffman, J.A. Sherman, E. Magnuson, B.B. Blinov, E.N. Fortson, Phys. Rev. A **85**, 043418 (2012). https://doi.org/10.1103/PhysRevA.85.043418
27. D.R. Leibrandt, M.J. Thorpe, M. Notcutt, R.E. Drullinger, T. Rosenband, J.C. Bergquist, Opt. Express **19**, 3471 (2011). https://doi.org/10.1364/OE.19.003471
28. P. Maddaloni, M. Bellini, P.D. Natale, *Laser-Based Measurements for Time and Frequency Domain Applications: A Handbook* (CRC Press). arXiv:org/abs/ftUTKFLCZboC
29. J. Sanjuan, K. Abich, M. Gohlke, A. Resch, T. Schuldt, T. Wegehaupt, G.P. Barwood, P. Gill, C. Braxmaier, Opt. Express **27**, 36206 (2019). https://doi.org/10.1364/OE.27.036206
30. X. Chen, Y. Jiang, B. Li, H. Yu, H. Jiang, T. Wang, Y. Yao, L. Ma, Chin. Opt. Lett. **18**, 030201 (2020)
31. S. Herbers, S. Häfner, S. Dörscher, T. Lücke, U. Sterr, C. Lisdat, Opt. Lett. **47**, 5441 (2022). https://doi.org/10.1364/OL.470984
32. M.L. Kelleher, C.A. McLemore, D. Lee, J. Davila-Rodriguez, S.A. Diddams, F. Quinlan, Opt. Express **31**, 11954 (2023). https://doi.org/10.1364/OE.486087
33. W. Zhang, M.J. Martin, C. Benko, J.L. Hall, J. Ye, C. Hagemann, T. Legero, U. Sterr, F. Riehle, G.D. Cole, M. Aspelmeyer, Opt. Lett. **39**, 1980 (2014). https://doi.org/10.1364/OL.39.001980
34. H. Shen, L. Li, J. Bi, J. Wang, L. Chen, Phys. Rev. A **92**, 063809 (2015). https://doi.org/10.1103/PhysRevA.92.063809
35. X. Shi, J. Zhang, X. Zeng, X. Lü, K. Liu, J. Xi, Y. Ye, Z. Lu, Appl. Phys. B **124**, 153 (2018). https://doi.org/10.1007/s00340-018-7021-y
36. J. Bi, Y. Zhi, L. Li, L. Chen, Appl. Opt. **58**, 690 (2019). https://doi.org/10.1364/AO.58.000690
37. W. Zhang, J.M. Robinson, L. Sonderhouse, E. Oelker, C. Benko, J.L. Hall, T. Legero, D.G. Matei, F. Riehle, U. Sterr, J. Ye, Phys. Rev. Lett. **119**, 243601 (2017). https://doi.org/10.1103/PhysRevLett.119.243601
38. J. Doyle, B. Francis, A. Tannenbaum, *Feedback Control Theory* (Macmillan Publishing, London, 1990)
39. R. Oswald, *Characterization and Control of a Cryogenic Ion Trap Apparatus and Laser Systems for Quantum Computing*, type Doctoral Thesis, school ETH Zurich (2022). https://doi.org/10.3929/ethz-b-000603723
40. P. Seiler, B. Hu, ECE 486: Control Systems (2021)
41. L. Li, W. Huie, N. Chen, B. DeMarco, J.P. Covey, Phys. Rev. Appl. **18**, 064005 (2022). https://doi.org/10.1103/PhysRevApplied.18.064005
42. A. Ryou, J. Simon, Rev. Sci. Instrum. **88**, 013101 (2017). https://doi.org/10.1063/1.4973470
43. P. Virtanen, R. Gommers, T.E. Oliphant, M. Haberland, T. Reddy, D. Cournapeau, E. Burovski, P. Peterson, W. Weckesser, J. Bright, S.J. van der Walt, M. Brett, J. Wilson, K.J. Millman, N. Mayorov, A.R.J. Nelson, E. Jones, R. Kern, E. Larson, C.J. Carey, İ Polat, Y. Feng, E.W. Moore, J. VanderPlas, D. Laxalde, J. Perktold, R. Cimrman, I. Henriksen, E.A. Quintero, C.R. Harris, A.M. Archibald, A.H. Ribeiro, F. Pedregosa, P. van Mulbregt, SciPy 1.0 Contributors. Nat. Methods **17**, 261 (2020). https://doi.org/10.1038/s41592-019-0686-2
44. H.W. Bode, Bell Syst. Tech. J. **19**, 421 (1940). https://doi.org/10.1002/j.1538-7305.1940.tb00839.x
45. J. Bechhoefer, Am. J. Phys. **79**, 1053 (2011). https://doi.org/10.1119/1.3614039. arXiv:1107.0071 [cond-mat, physics:physics]
46. T. Preuschoff, P. Baus, M. Schlosser, G. Birkl, Rev. Sci. Instrum. **93**, 063002 (2022). https://doi.org/10.1063/5.0093520
47. G.D. Domenico, S. Schilt, P. Thomann, Appl. Opt. **49**, 4801 (2010). https://doi.org/10.1364/AO.49.004801
48. N.V. Bandel, M. Myara, M. Sellahi, T. Souici, R. Dardaillon, P. Signoret, Opt. Express **24**, 27961 (2016). https://doi.org/10.1364/OE.24.027961
49. Z. Bai, Z. Zhao, Y. Qi, J. Ding, S. Li, X. Yan, Y. Wang, Z. Lu, Front. Phys. **9** (2021)
50. J.-Q. Chen, C. Chen, J.-J. Sun, J.-W. Zhang, Z.-H. Liu, L. Qin, Y.-Q. Ning, L.-J. Wang, Sensors **24**, 3656 (2024). https://doi.org/10.3390/s24113656
51. W.C. Wang, in preparation (2025)
52. T.C. Briles, D.C. Yost, A. Cingöz, J. Ye, T.R. Schibli, Opt. Express **18**, 9739 (2010). https://doi.org/10.1364/OE.18.009739

53. T. Nakamura, S. Tani, I. Ito, M. Endo, Y. Kobayashi, Opt. Express **28**, 16118 (2020). https://doi.org/10.1364/OE.390042
54. J. Alnis, A. Matveev, N. Kolachevsky, Th. Udem, T.W. Hänsch, Phys. Rev. A **77**, 053809 (2008). https://doi.org/10.1103/PhysRevA.77.053809
55. I. Sherstov, M. Okhapkin, B. Lipphardt, C. Tamm, E. Peik, Phys. Rev. A **81**, 021805 (2010). https://doi.org/10.1103/PhysRevA.81.021805
56. V. Mackowiak, J. Peupelmann, Y. Ma, A. Gorges, NEP: Noise Equivalent Power (2015)
57. J. Bai, J. Wang, J. He, J. Wang, J. Opt. **19**, 045501 (2017). https://doi.org/10.1088/2040-8986/aa5a8c
58. T. Rabga, K.G. Bailey, M. Bishof, D.W. Booth, M.R. Dietrich, J.P. Greene, P. Mueller, T.P. O'Connor, J.T. Singh, Opt. Express **31**, 41326 (2023). https://doi.org/10.1364/OE.500578
59. J. Tu, A. Restelli, T.-C. Tsui, K. Weber, I.B. Spielman, S.L. Rolston, J.V. Porto, S. Subhankar, Quadrature amplitude modulation for electronic sideband Pound–Drever–Hall locking (2024). arXiv:2409.08764 [cond-mat, physics:physics]
60. R.A. Hildebrand, A. Restelli, W. Wang, C. Goham, J.W. Britton, Spectrally-pure optical Serrodyne modulation for continuously-tunable laser offset locking (2024). arXiv:2412.05411 [quant-ph]
61. D.Z. Anderson, Appl. Opt. **23**, 2944 (1984). https://doi.org/10.1364/AO.23.002944
62. J.A. Boyd, T. Lahaye, Am. J. Phys. **92**, 50 (2024). https://doi.org/10.1119/5.0161369
63. MOGlabs, AN002: Pound–Drever–Hall Locking with the FSC (2019)
64. FALC pro: Digitally controlled fast laser locking module. https://www.toptica.com/products/tunable-diode-lasers/laser-locking-electronics/falc-pro()
65. Products or companies named here are included in the interest of completeness and does not imply endorsement by the authors or by the us government. Stop
66. O. Mor, A. Arie, IEEE J. Quantum Electron. **33**, 532 (1997). https://doi.org/10.1109/3.563380
67. D.R. Leibrandt, J. Heidecker, An open source digital servo for AMO physics experiments (2015). arXiv:1508.06319 [physics]
68. S.J. Yu, E. Fajeau, L.Q. Liu, D.J. Jones, K.W. Madison, Rev. Sci. Instrum. **89**, 025107 (2018). https://doi.org/10.1063/1.5001312
69. A. Tourigny-Plante, V. Michaud-Belleau, N. Bourbeau Hébert, H. Bergeron, J. Genest, J.-D. Deschênes, Rev. Sci. Instrum. **89**, 093103 (2018). https://doi.org/10.1063/1.5039344
70. M.A. Luda, M. Drechsler, C.T. Schmiegelow, J. Codnia, Rev. Sci. Instrum. **90**, 023106 (2019). https://doi.org/10.1063/1.5080345
71. B. Wiegand, B. Leykauf, R. Jördens, M. Krutzik, Rev. Sci. Instrum. **93**, 063001 (2022). https://doi.org/10.1063/5.0090384
72. L. Neuhaus, M. Croquette, R. Metzdorff, S. Chua, P.-E. Jacquet, A. Journeaux, A. Heidmann, T. Briant, T. Jacqmin, P.-F. Cohadon, S. Deléglise, Rev. Sci. Instrum. **95**, 033003 (2024). https://doi.org/10.1063/5.0178481
73. N. Jin, C.A. McLemore, D. Mason, J.P. Hendrie, Y. Luo, M.L. Kelleher, P. Kharel, F. Quinlan, S.A. Diddams, P.T. Rakich, Optica **9**, 965 (2022). https://doi.org/10.1364/OPTICA.467440
74. J. Guo, C.A. McLemore, C. Xiang, D. Lee, L. Wu, W. Jin, M. Kelleher, N. Jin, D. Mason, L. Chang, A. Feshali, M. Paniccia, P.T. Rakich, K.J. Vahala, S.A. Diddams, F. Quinlan, J.E. Bowers, Sci. Adv. **8**, eabp9006 (2022). https://doi.org/10.1126/sciadv.abp9006
75. S. Häfner, S. Falke, C. Grebing, S. Vogt, T. Legero, M. Merimaa, C. Lisdat, U. Sterr, Opt. Lett. **40**, 2112 (2015). https://doi.org/10.1364/OL.40.002112
76. Fabry-Perot Cavities. https://stablelasers.com/fabry-perot-cavities/
77. FALC 110 and mFALC 110: Fast laser locking module. https://www.toptica.com/products/laser-rack-systems/laser-locking-electronics/falc-110-mfalc-110-fast-pid()
78. DL pro. https://www.toptica.com/products/tunable-diode-lasers/ecdl-dfb-lasers/dl-pro
79. S. Schmidt-Eberle, Linewidth Measurement of Diode Lasers (2023)
80. N. Kolodzie, I. Mirgorodskiy, C. Nölleke, P.O. Schmidt, Opt. Express **32**, 29781 (2024). https://doi.org/10.1364/OE.530087
81. R. Kervazo, A. Congar, G. Perin, L. Lablonde, R. Butté, N. Grandjean, L. Bodiou, J. Charrier, S. Trebaol, Sub-20 kHz low frequency noise near ultraviolet miniature external cavity laser diode (2024). arXiv:2405.15462
82. M. Houssin, M. Jardino, M. Desaintfuscien, Rev. Sci. Instrum. **61**, 3348 (1990). https://doi.org/10.1063/1.1141582
83. M.J. Lawrence, B. Willke, M.E. Husman, E.K. Gustafson, R.L. Byer, J. Opt. Soc. Am. B JOSAB **16**, 523 (1999). https://doi.org/10.1364/JOSAB.16.000523